Detailed comparison of theory and experiment of strong-field photodetachment of the negative hydrogen ion

Rainer Reichle, Hanspeter Helm, and Igor Yu. Kiyan

Physikalisches Institut, Albert-Ludwigs-Universität, D-79104 Freiburg, Germany

We study the strong-field interaction of a negative hydrogen ion in a short infrared laser pulse. An imaging technique is employed in a fast ion beam to record angular-resolved energy distributions of the photodetached electrons. The spectrum exhibits four excess photon channels. A detailed analysis of the energy and angular distribution is presented, including a comparison with recent theories. From our data we determine elastic-scattering phase shifts of the partial continuum waves in the lowest-order detachment channel. Quantitative agreement with scattering theory is obtained. A quantum interference effect predicted in a recent Keldysh-like theory is observed at energies close to threshold. We propose an analogy to a double-slit model which explains the interference features in a simple and intuitive way. We also verify the applicability of the Wigner threshold law in the strong-field regime and discuss its role in the observed quantum interference.

PACS number(s): 32.80.Rm, 32.80.Gc

I. INTRODUCTION

Atomic or molecular systems exposed to intense laser fields show above threshold ionization (ATI), a multiphoton ionization process that involves more than the necessary number of photons to reach the continuum [1,2]. ATI occurs at field strengths well below the inner atomic field. Several distinct, nonperturbative approaches have been developed for its description. Among these are direct numerical integration methods (see Sec. III G of Ref. [2]), the Keldysh-Faisal-Reiss (KFR, Refs. [3–5]) method and its various modifications [6,7], and complex quasienergy methods [8,9].

From the standpoint of theory, negative ions constitute simpler systems than neutral atoms due to the lack of suitable intermediate states for resonantly enhanced ionization. In addition, the atomic potential for negative ions can, to a first approximation, be modeled by a zero-range potential. This approximation allows a pure analytical description in the form of a Keldysh-like theory [6]. In unraveling the inherent ionization dynamics this approximation turns out to be rather practicable as it expands the multiphoton transition matrix element in complex trajectories in the formalism of path integrals. The dynamics of the electron is thus related to a coherent superposition of quantum trajectories.

Strong-field ionization of the weakly bound electron in a negative ion represents one of the rare cases in which only a small number of such paths contribute to the dynamics [10,11]. We show here that the quantum path interference of a single electron can be observed by exposing negative ions to a linearly polarized, intense laser field. In fact this interference dominates angular distributions (ADs) at low electron energies, preventing under certain conditions any photodetachment along the laser polarization axis. This counterintuitive behavior has also been predicted in recent theoretical works by Borca *et al.* [8] and by Telnov and Chu [9].

Experimental investigations of negative ions in intense laser fields are limited [12–14] since they must first be prepared and properly isolated from their neutral parent to specify the initial state. The observation of excess photon detachment (EPD) in H^-, the analogous process to ATI for negative ions, was found to be difficult because of the small binding energy of the outer electron and the high laser intensity required [15,16]. A major difficulty lies in the finite rise time of the laser pulse which leads to depletion of the H^- bound state population prior to reaching the peak intensity. We show here that this problem can be circumvented by using long wavelength radiation and ultrashort laser pulses. Our work tests the applicability of Keldysh-like approaches over a wide range of phase space of the continuum electron and examines the profound role of quantum path interferences in the detachment dynamics of a negative ion.

II. EXPERIMENT

Our experimental setup is shown in Fig. 1. H^- ions are formed in a hollow cathode discharge, accelerated to 3 keV and mass selected. Einzel lenses control the focusing of the ion beam in the interaction region, where the beam waist is 400 μm at a flux of 100 nA. The 90° bend in the quadrupole serves to clean the negative-ion beam from neutral atoms formed by collisional detachment in the first two vacuum sections. Three differentially pumped sections maintain a residual pressure of 5×10^{-10} mbar in the interaction region during operation. Laser pulses of an energy of 56 μJ, a pulse length of 250 fs [full width at half maximum (FWHM)], and a wavelength of 2.15 μm are generated in an optical parametric amplifier pumped with a Ti:sapphire laser system at a repetition rate of 1 kHz. The laser beam is focused by a 15- cm focal length lens and crosses the ion beam at right angle. The intensity distribution in the laser focus is measured by scanning a razor blade across the focus. It can be well reproduced by a Gaussian shape with a waist of 50 μm (FWHM) and a Rayleigh range of 4 mm. The peak intensity in the laser focus is of the order of 1.7×10^{13} W/cm^2.

The central part of our setup is an imaging spectrometer [17], which maps electrons ejected in the entire solid angle onto a two-dimensional (2D) position sensitive detector by an electrostatic field. The position sensitive detector consists
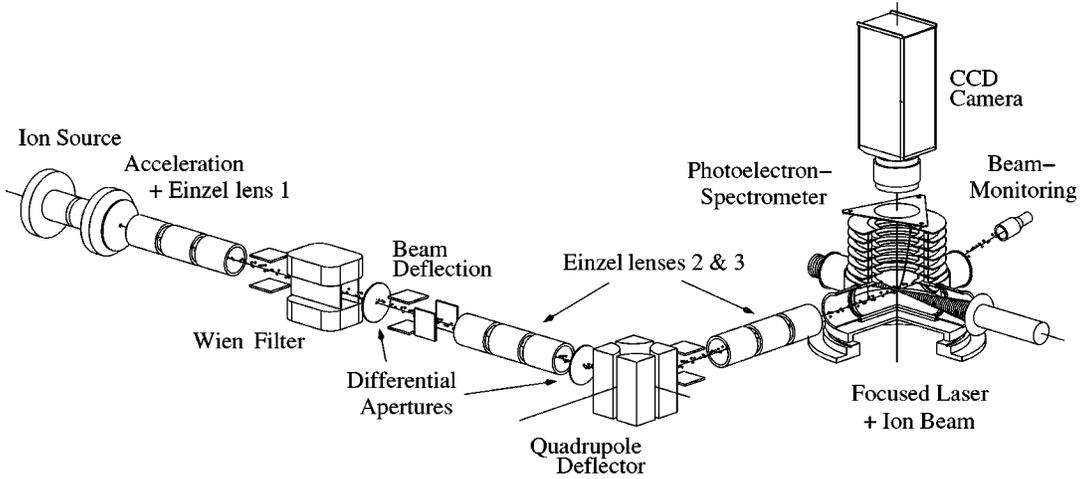
FIG. 1. Schematic view of the negative-ion beam apparatus. Details are given in the text.

of a stack of image-quality multichannel plates and a home-made phosphor screen, coated on a glass plate with a transparent conductive gold layer. The light spots are imaged onto a charge-coupled-device array (12-bit resolution) where they are accumulated and retrieved by a frame grabber at intervals of a few minutes. A Wollaston prism polarizer ensured linear polarization, oriented parallel to the detector surface. The spectrometer is operated in the velocity mapping regime [18] which we discuss in the following section. The last vertical pair of steering plates precompensates the small deflection of negative ions towards the interaction region by the projection field of the imaging spectrometer. This ensures a nearly horizontal beam path across the laser focus, an important requirement to suppress asymmetry of the photoelectron image. Residual electron background is reduced by pulsing the ion beam with 10 μs on and 990 μs off for each laser shot period. Under typical operating conditions about 5 events per laser shot are recorded. Distortions by space charge effects do not occur at such an electron yield.

The drift energy of photoelectrons formed in an n-photon transition by a short laser pulse is defined as (in atomic units)

$$E_{p_n} = p_n^2/2 = n\,\omega + E_0 - \alpha_0(\omega)F^2/4 - F^2/4\omega^2. \quad (1)$$

Here p_n is the electron momentum, ω and F are the frequency and the electric-field strength of laser radiation, respectively. E_0 is the binding energy of the negative hydrogen ion ($-0.754\,21$ eV [19]). The last two terms in Eq. (1) correspond to the ac Stark shift of the ground state of H$^-$ and the ponderomotive shift of the continuum threshold, respectively. The dynamical polarizability $\alpha_0(\omega)$ is described in Ref. [20] and its value is ≈ 270 a.u. at our laser frequency. Equation (1) is valid for our short laser-pulse condition, in which case the ponderomotive acceleration of electrons from the focal volume can be neglected.

III. ELIMINATION OF IMAGE DISTORTIONS

The spatial distribution of photoelectrons moving towards the detector under the action of the projection field can be represented by a superposition of expanding concentric spheres. Each sphere describes electrons of a particular momentum value p_n and its radius is defined as $r = p_n t/m_e$, where t is the expansion time. The modulation of the electron density over the sphere is determined by the angular dependence of the photodetachment probability at the given electron momentum. For linearly polarized electromagnetic field, the angular distribution has a cylindrical symmetry and represents a function of solely the angle θ between the electron momentum vector and the laser polarization axis.

Here we consider two intrinsic sources of image distortion by comparing simulated maps of a single sphere onto the detector plane. Ideal imaging is achieved when the sphere is mapped in a parallel projection as indicated in Fig. 2(a). In this case, each parallel of latitude is projected into a single line in the detector plane.

Distortions arise because of the finite time Δt of the sphere projection. While the front part of the sphere is already mapped onto the detector, its back part continues to expand during this time interval. The value of Δt can be defined by dividing the diameter of the sphere by the velocity of its center, v, at the location of the detector. Thus, $\Delta t = 2v_0 T/v$, where T denotes the time of flight of an electron with zero initial energy from the origin to the detector, and $v_0 = p_n/m_e$ is the initial electron velocity. The influence of this distortion decreases with smaller values of the ratio $\Delta t/T$. This ratio is related to a parameter ρ which represents the ratio of the energy gained by the electron in the projection field and the initial drift energy E_{p_n}:

$$\Delta t/T = 2/\sqrt{\rho}. \quad (2)$$

The parameter ρ is therefore a measure of the quality of the projected image. Images for three different values of ρ are compared in Fig. 2(b). For large values of ρ the parallels of latitude are projected into narrow ellipses, approximating the ideal case of straight lines [21].

Another distortion arises from the translational motion of the negative-ion target. Ejection from a moving target sweeps the spheres across the detector surface in the direction of the translation during the projection time Δt. This
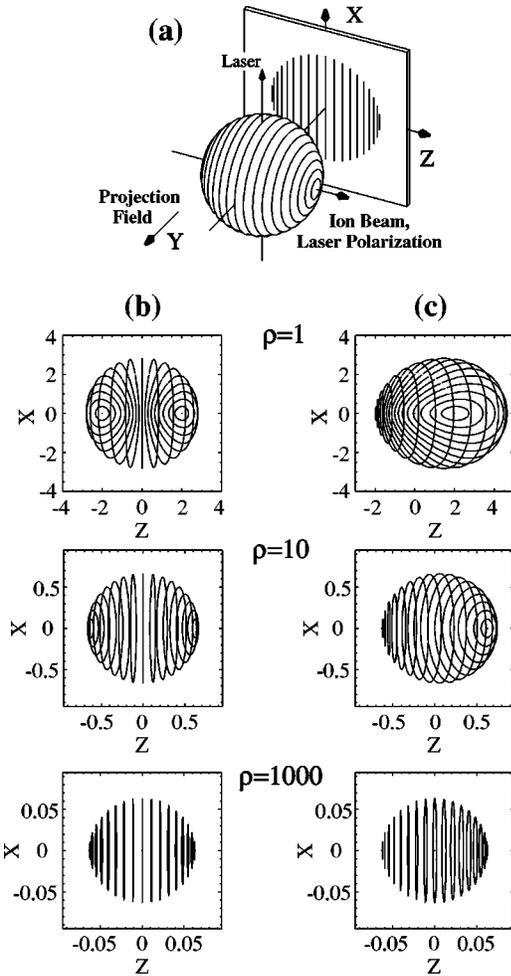
FIG. 2. (a) Definition of ideal imaging conditions (parallel projection), (b) distortions due to finite projection time when the ion target is at rest, and (c) finite projection time distortions when the target has an additional translational motion (assumed here to be equal to v_0). The X-Z plots show how parallels of latitude on the sphere are projected as a function of the imaging parameter ρ. The quality of our measurement corresponds to $\rho \approx 1000$. Calculations are based on classical trajectory solutions in a homogeneous projection field.

complication is illustrated in Fig. 2(c) for the particular case when the velocity of the target ion is identical to the velocity v_0 of the emitted electron. In this case backwards emitted electrons have zero kinetic energy.

Both distortion effects can be significantly reduced by choosing ρ to be large, as may be seen from Fig. 2. This situation may be named "hard projection." The value of ρ controls the size of the image on the detector, a larger ρ value implying an image of smaller dimension. However, it is possible to achieve a predefined quality value ρ *and* an appropriate size of the image by choosing a long enough flight distance. In our experiment we achieve a quality value $\rho \approx 1000$ at a typical image diameter of ≈ 1 cm. In order to demonstrate the sufficient improvement in the image quality at such a high value ρ, a test experiment was performed where we recorded p-wave photoelectrons produced by one-photon detachment in a weak field of the fundamental of the
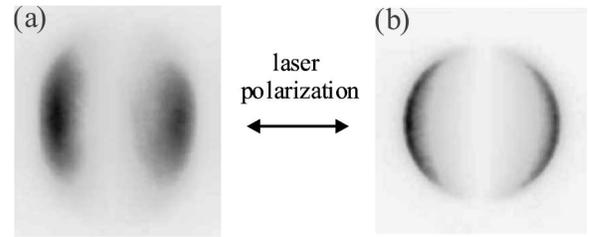

FIG. 3. Raw images of one-photon detachment of H$^-$ in a weak field of 796 nm recorded by using a homogeneous projection field of moderate quality $\rho \approx 30$ (a) and by using a hard projection with $\rho \approx 1000$ in the velocity mapping regime (b). Both images show a signal of p-wave electrons with the kinetic energy of 0.804 eV. All image distortions discussed in the text are clearly visible in (a).

Ti:sapphire laser ($\lambda = 796$ nm). Figure 3 gives two examples of images, one taken with a moderate projection quality ($\rho \approx 30$) and a flight distance of 16 mm, and one by employing a hard projection ($\rho \approx 1000$) with a five times longer flight distance. The two distortion effects discussed above are apparent from Fig. 3(a). As a consequence of the finite time of projection and the translation of the target a broadening of the outer rim and a forward-backward-asymmetry appear. A closer inspection of the image in Fig. 3(a) also reveals that it is not circular but elongated along the laser beam propagation direction. This is because of a finite size of the interaction volume which extends in this dimension over the 400 μm width of the ion beam (note that the Rayleigh range of the laser focus is much larger than this value). The two other dimensions of the interaction volume are defined by the waist of the laser focus of 50 μm, which is smaller than the spatial resolution of our detector (≈ 100 μm). In order to avoid the elongation, we employed a slightly nonuniform projection field which operates in the form of an electrostatic immersion lens (for details, see Ref. [22]). In this case trajectories of electrons starting with the same velocity vector at different lateral positions in the interaction volume merge at a single point on the detector. The improvement in the image quality obtained with the use of this velocity mapping [18] is evident from Fig. 3(b), where the image appears circular.

IV. EXPERIMENTAL IMAGE AND IMAGE PROCESSING

Employing a hard projection in combination with the velocity mapping regime, the image shown in Fig. 4 was recorded by using strong laser radiation at the wavelength of 2.15 μm. The data were accumulated over a period of 3 h, corresponding to $\sim 10^8$ detected electrons. To avoid long-term drifts this time was divided into equal periods with the laser off and on. The background images (laser off) are subtracted to discriminate the signal of collisionally induced electrons. The electron image in Fig. 4 is smooth and highly structured. Note that no smoothing routine is applied to these data. They cover a pixel area of $\approx 150 \times 150$ at a dynamic range of $\approx 2 \times 10^3$.

The system of rings in Fig. 4 corresponds to different n-photon channels according to the proportionality $r \propto p_n$. The polar modulation of the electron yield at a given radius
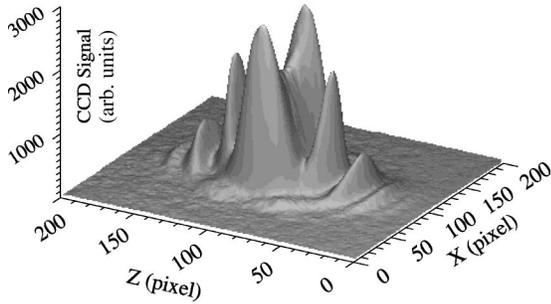
FIG. 4. Raw image of photoelectrons produced in a laser field of 2.15 μm wavelength and 1.7×10^{13} W/cm^2 peak intensity. The image corresponds to $\sim 10^8$ detected electrons.

renders the angular distribution at a corresponding value of the electron momentum. Nodes indicate the dominance of specific partial waves describing the outgoing electron. A quantitative analysis of the differential detachment rates is performed below in two steps. First, the recorded image is numerically inverted in order to reconstruct the 3D photoelectron distribution before projection. In a second step, the data are corrected for the detector resolution. An absolute calibration of the momentum scale of the detector is also carried out.

A. Backprojection

It is evident from Fig. 2 that under hard projection conditions the reconstruction of the 3D distribution separates into inversions of lower dimensionality. In this case an inversion of each separate pixel row in Fig. 2 results in a 2D slice of the 3D distribution. This inversion corresponds to an Abel transform [23]. A drawback of such a 1D backprojection routines of a discrete set of pixels is that they accumulate numerical errors along the symmetry axis $X=0$. In order to avoid this we applied the approach of Vrakking [24], which is based on an Abel inversion and a subsequent 2D correction employing a quasifitting algorithm. Numerical errors in this approach are contracted at the unessential center of the image $X=Z=0$, corresponding to zero electron kinetic energy. In a first approximation this algorithm reconstructs the 3D radial and angular distribution using an Abel inversion for each pixel row. In a second step this trial distribution is numerically forward projected and compared with the raw data. The difference obtained this way is used in an iterative correction for every angular and radial point. After each iteration a χ^2-test decides for continuation or abortion of the correction procedure.

B. Energy calibration and deconvolution

We calibrated the detector scale in the momentum representation by recording images of the p-wave one-photon detachment at three known wavelengths, the fundamental of the Ti:sapphire laser, its second harmonic, and a dye laser wavelength of 591.3 nm [see Fig. 3(b) for an example]. In each case laser radiation was strongly attenuated to make the ponderomotive shift of the continuum threshold negligible. The corresponding photoelectron kinetic energies are 0.804,

2.363, and 1.347 eV, respectively. The calibration images were backprojected by using the routine described above. We obtained a linear relation between the radii of reconstructed spheres and the expected electron momenta with a calibration coefficient of $0.976(3) \times 10^6$ m/s per pixel. The radial profile of a backprojected calibration image defines the apparatus function of the detector. We found it to be equivalent to the finite spatial resolution of the single event response of the detector. This function can be described by a Voigt profile with a FWHM of 7.5 pixels.

The Voigt response function was used to deconvolve the (p, θ) distribution obtained as a result of backprojection of the raw image shown in Fig. 4. Here p denotes the calibrated momentum coordinate. Since the angular dependence contains no sharp features over the width of a few pixels, the deconvolution is solely performed along the momentum coordinate. The convolution is described by a Fredholm integral equation

$$h_i(p) = \int K(p, p') f_i(p') dp'. \tag{3}$$

The kernel $K(p, p')$ represents the experimentally defined response function expressed in the momentum representation and p' denotes the momentum coordinate of the deconvoluted image. The function $h_i(p)$ is the measured momentum distribution at a given angle step i and $f_i(p)$ is to be determined. A typical feature of such an "ill-posed" problem is that the deconvoluted image accumulates an oscillatory structure caused by statistical noise. This problem can be overcome by using a Tikhonov regularization routine [26]. The regularization procedure was carried out for discrete emission angles θ_i at a step size of $4°$. The deconvoluted (p, θ) distribution was converted into the (E, θ) spectrum, where E represents the kinetic-energy scale. The final result is shown in the upper part of Fig. 5.

V. COMPARISON WITH A KELDYSH-LIKE THEORY

Similar to the original work by Keldysh [3] and Perelomov et $al.$ [28], the adiabatic approach by Gribakin and Kuchiev [6] uses the saddle-point method to evaluate the transition matrix element in a linearly polarized field $F(t) = F \cos \omega t$. The transition amplitude represents the sum of two contributions corresponding to the saddle points $\mu = 1,2$ of the classical action in the plane of complex time:

$$\mathcal{A}_{pn} = \sum_{\mu=1,2} \frac{(c_\mu + i s_\mu)^n}{\sqrt{2\pi(-i S''_\mu)}} \exp[-i c_\mu (\xi + z s_\mu)], \tag{4}$$

where

$$s_\mu = [-\xi \pm i\sqrt{8z(n-z) - \xi^2}]/4z, \quad c_\mu = \pm\sqrt{1 - s_\mu^2},$$

$$S''_\mu = c_\mu(\xi + 4z s_\mu), \quad z = e^2 F^2/4\omega^3, \quad \xi = eFp\cos\theta/\omega^2.$$

The $\pm$ signs correspond to $\mu = 1,2$, respectively. The amplitude in Eq. (4) is in the familiar path-integral formalism (see Ref. [10], and references therein) which enables an interpretation in terms of complex trajectories. The real part of a
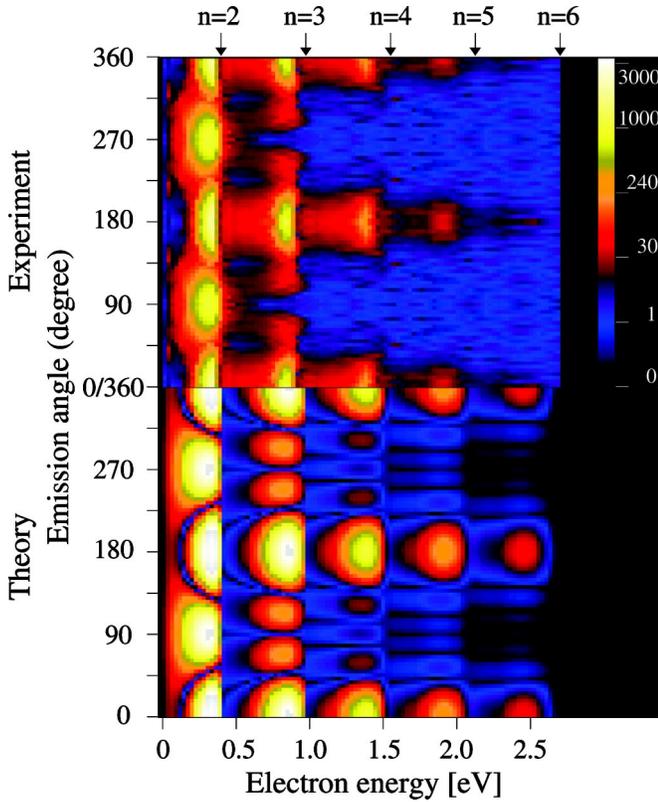
FIG. 5. (Color online) Photoelectron spectrum as a function of drift energy and emission angle: upper part—experiment, lower part—simulation by using a Keldysh-like theory (see text). The spectra are normalized according to the integrated signal. The color scale factor is in arbitrary units.

complex trajectory may be considered as the classical path, while the imaginary part is related to a measure of its relative weight [11]. The coherent superposition of two saddle points in Eq. (4) gives rise to interference between the two associated quantum trajectories. Using Eq. (4) for the transition amplitude, the differential rate for the n-photon detachment channel is [6]

$$\frac{dw_n}{d\Omega} = \frac{3A^2}{4\pi} p \, |\mathcal{A}_{pn}|^2, \qquad (5)$$

where $A = 0.75$ is a normalization coefficient of the asymptotic wave function of the ground state of H^-.

A. Saturation, focal volume, and ponderomotive shift

In order to compare the angular and momentum distribution calculated from Eqs. (4) and (5) with the experimental values, the following experimental circumstances need to be taken into account. Because of the spatial and temporal distribution of laser intensity in the focus, negative ions experience different field strengths in the range from zero to the peak value. Thus, the photodetachment rate must be integrated over the intensity distribution. On doing this, the ponderomotive shift should be taken into account. Since the ponderomotive shift is proportional to the laser intensity, this integration results in a broadening of the energy peaks. In

addition, the saturation of the photodetachment process (depletion of the primary ions) needs to be taken into account. It effectively reduces the peak intensity experienced by negative ions. We found that this effect is sensitive to the temporal profile of the laser pulse assumed. The best agreement between the experimental and simulated spectra is achieved with a $\text{sech}^2(t)$ profile. This is also consistent with the measured autocorrelation trace of the temporal laser profile. Since the Rayleigh range of the laser focus is much larger than the spot size of the ion beam, the interaction volume can be approximated by a cylinder where the intensity dependence on its radial coordinate r needs to be considered. Thus, the spatial and temporal shape of the laser pulse in the focus is represented by

$$I(r,t) = I_{peak} \, e^{-(r/\sigma_r)^2} \text{sech}^2\!\left(\frac{t-t_0}{\sigma_t}\right), \qquad (6)$$

where $\sigma_t = 250$ fs and the focus waist $\sigma_r = 50$ μm according to our beam diagnostic measurements. The value of the peak intensity I_{peak} is obtained by normalizing the integral of $I(r,t)$ over r and t to the pulse energy delivered into the interaction region.

For a given radial coordinate r and time t the n-photon yield of photoelectrons per unit time and unit volume of interaction is defined as the product of the differential rate and the population of negative ions in the ground state:

$$y_n(\theta,r,t) = g(r,t) \frac{d}{d\Omega} w_n(\theta,I(r,t)). \qquad (7)$$

Taking depletion into account, the ground-state population is

$$g(r,t) = g_0 \exp\left\{ -\sum_n \int_{-\infty}^{t} d\tau w_n(I(r,\tau)) \right\}, \qquad (8)$$

where g_0 is the initial density of negative ions and w_n is the n-photon detachment rate integrated over the solid angle. A simulated (E,θ) electron distribution is obtained by integrating Eq. (7) over the radial coordinate r and time t, and adding together contributions from different n-photon channels:

$$\frac{d\Gamma}{d\Omega}(E,\theta) \propto \sum_n \int_0^{\infty} dr \, r \int_{-\infty}^{\infty} dt \, y_n(\theta,r,t)$$
$$\times \delta(n\omega - E - \tau I(r,t) + E_0). \qquad (9)$$

Here the δ function accounts for the ponderomotive shift of the continuum and the ac Stark shift of the ground state, and $\tau = [\alpha_0(\omega) + 1/\omega^2]/4 = 623.7$ a.u. Since $\alpha_0(\omega)\omega^2 \sim 1/10$ for the frequency used in our experiment, the ground-state shift is of minor importance and is neglected in these calculations. The simulated spectrum is presented in the lower part of Fig. 5 [27].

VI. DISCUSSION

Below we analyze the experimental and theoretical spectra in Fig. 5. Both spectra reveal four distinct EPD channels broadened by the ponderomotive effect. Energy limits E_n

$=n\omega+E_0$ for vanishing intensity are indicated by arrows together with the respective photon numbers. Since the different photon channels are well separated in energy we can analyze each channel individually. Then, electrons of a given energy E can be unambiguously assigned to a particular n-photon channel, and the measured ponderomotive shift $U_p=E_n-E$ can be used to define the intensity value at which these electrons are produced, $I=4\omega^2 U_p$. It enables to analyze angular distributions in a given channel as a function of the laser field strength.

A. Lowest-order channel and threshold effects

Figure 6 shows polar plots of the experimental ADs in the two-photon channel at different kinetic energies between the threshold and the unshifted energy $E_2=399.1$ meV. Recently Wang and Elliott have shown that ADs of multiphoton ionization allow a direct experimental insight into the elastic scattering phase shift [29]. In a similar way, our data allow to extract complex partial-wave amplitudes of the final continuum state as a function of electron energy. The ADs are fitted to the partial-wave decomposition of the n-photon detachment rate

$$\frac{d\Gamma_n}{d\Omega} \propto |f_{P_n}(\theta)|^2, \quad f_{P_n}(\theta)=\sum_{L=0}^{L_{\max}} f_L^{(n)} Y_{L0}(\theta,\phi), \quad (10)$$

where L denotes the angular momentum of the outgoing electron and Y_{L0} is the corresponding spherical harmonic. Only terms with zero projection of the angular momentum contribute to the sum, as it should be in the case of linear polarization and isotropic initial state. The complex amplitudes $f_L^{(n)}$ are determined in the fit. For a given EPD channel, the parity of the final state is defined by the number n of absorbed photons, and either odd or even L contributes to the sum in Eq. (10). The number of fitting parameter is $L_{\max}$ or $L_{\max}+1$ for odd or even final-state parity, respectively.

For two-photon detachment of H$^-$ a superposition of s and d waves is expected. In a strong laser field, however, stimulated reemission of photons from higher channels might be significant to induce higher angular momenta. In order to explore this effect the sum in Eq. (10) is extended to $L_{\max}=4$, allowing for a g-wave contribution. The right column in Fig. 6 compares fitted and experimental polar plots. Circles represent experimental data and solid lines are the fit result. The inner solid lines illustrate the analogous fit to the simulated data shown in the lower part of Fig. 5. For visual convenience the latter are scaled by a factor of 0.8. One can see from Fig. 6 that the simulation results reproduce well the experimental data.

In the lowest-order channel the ADs undergo strong modifications close to threshold. At low kinetic energies the Wigner law [30] predicts the partial-wave amplitudes to have the energy dependence $|f_L^{(2)}|^2 \propto E^{L+1/2}$. According to this dependence, the s wave dominates near threshold, a tendency which is indeed observed in the experiment. The three plots in Fig. 6 for electron energies of 163, 136, and 108 meV show how the nodal cone of the d wave is gradually eliminated due to the increasing s wave contribution. Experimen-

F ~ 0.0022 a.u.
E ~ 325 meV

F ~ 0.0029 a.u.
E ~ 271 meV

F ~ 0.0035 a.u.
E ~ 217 meV

F ~ 0.0040 a.u.
E ~ 163 meV

F ~ 0.0042 a.u.
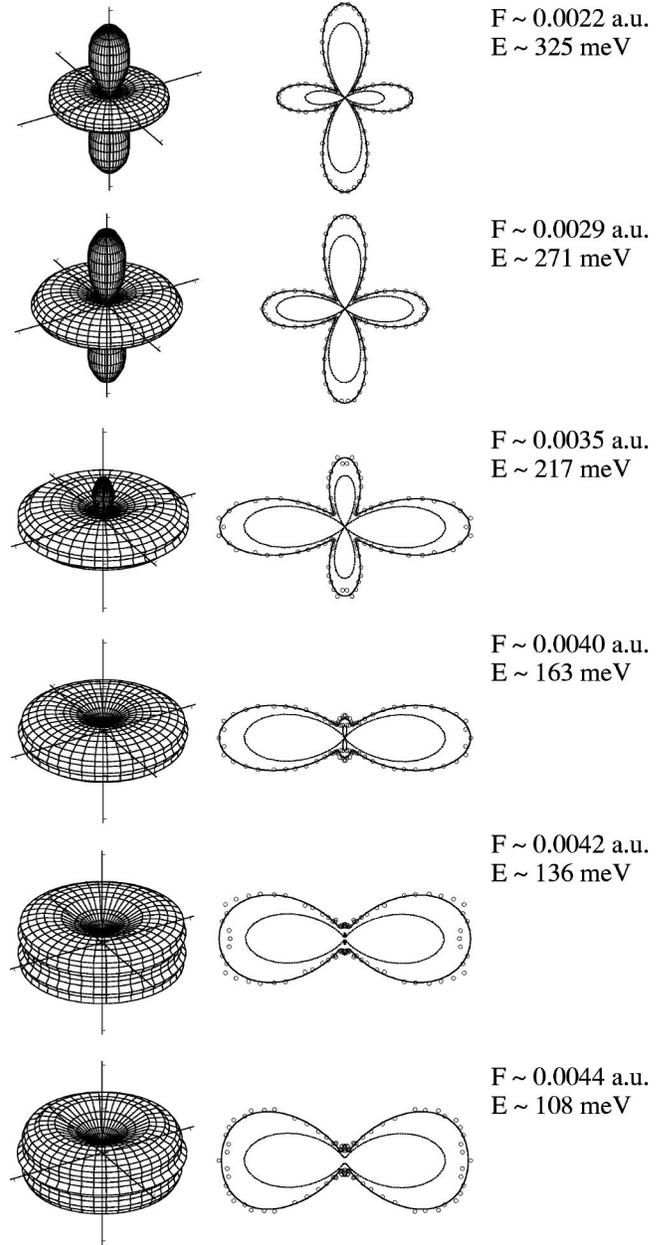E ~ 136 meV

F ~ 0.0044 a.u.
E ~ 108 meV

FIG. 6. Experimental and theoretical angular distributions for the two-photon channel. The laser polarization is oriented vertically in the graph. The dependence of the ADs on the laser intensity is shown from the top to the bottom with increasing field strength (decreasing electron energy). The left column shows experimental ADs in 3D. The right column compares the experimental data with a fit (circles and outer solid line) and the inner solid lines represent the calculated ADs from Fig. 5 (lower spectrum). The calculated curves are multiplied by a factor 0.8 for visual convenience.

tal ADs at even lower kinetic energies have worse signal-to-noise ratio and are not shown. Instead, we refer here to the simulated spectrum in Fig. 5, where the isotropic angular distribution near threshold can be clearly seen.

In view of this discussion, it is interesting to show that the Wigner law can be derived from the Keldysh-like theory. In the limit of low kinetic energies $E\ll|E_0|$ the n-photon detachment rate from a state of angular momentum ℓ acquires
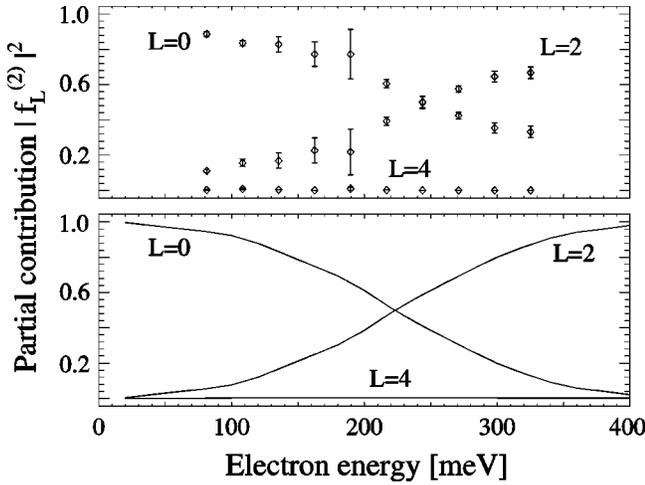
FIG. 7. Partial-wave contributions in the two-photon channel. The sum of contributions is normalized to unity. Upper and lower parts refer to the analysis of the experimental and theoretical spectra in Fig. 5, respectively.

the form [Eq. (42) of Ref. [6]]

$$\frac{dw_n}{d\Omega} \propto p \exp\left[\left(-\sinh^{-1}\gamma + \frac{\gamma\cos^2\theta}{\sqrt{\gamma^2+1}}\right)\frac{p^2}{\omega}\right]$$
$$\times \left\{1 + (-1)^{n+\ell}\cos\left(\frac{2\kappa p \cos\theta\sqrt{\gamma^2+1}}{\omega\gamma}\right)\right\}, \quad (11)$$

where $\gamma = \kappa\omega/F$ is the Keldysh parameter, $\kappa^2 = -E_0$, and only terms dependent on p and θ are considered. When the value of p is close to zero, the above expression can be expanded into a Taylor series over p. Leaving the first significant term in the expansion we obtain a detachment rate proportional to p when $n+\ell$ is even and proportional to $p^3\cos^2(\theta)$ when $n+\ell$ is odd. This is exactly the prediction of the Wigner threshold law.

For a quantitative comparison we present in Fig. 7 the energy dependence of the squared moduli of the normalized partial-wave amplitudes for the experimental and the theoretical data. The *g*-wave contribution turns out to be very small in both datasets. Hence, stimulated reemission of photons is only a minor path in the lowest-order detachment channel. The main source of error in the experimental data is due to the uncertainty in the background signal from which we estimated the error bars in Fig. 7. An additional contribution to the error bars arises from systematic errors in the data processing. The disagreement with the theoretical data at energies close to the unshifted limit of $2\omega + E_0$ is attributed to a failure of the deconvolution process due to the steep slope of the signal in this region. Quantitative agreement is obtained in the lower-energy part of the two-photon channel.

The amplitudes $f_0^{(2)}$ and $f_2^{(2)}$, as complex numbers, can be represented in terms of their absolute values and phases. These phases are identical to the elastic-scattering phases, δ_0 and δ_2, which describe the *s*- and *d*-wave electron scattering on the neutral hydrogen atom [31]. Thus, our data can be compared with results from scattering theory. From the fit,
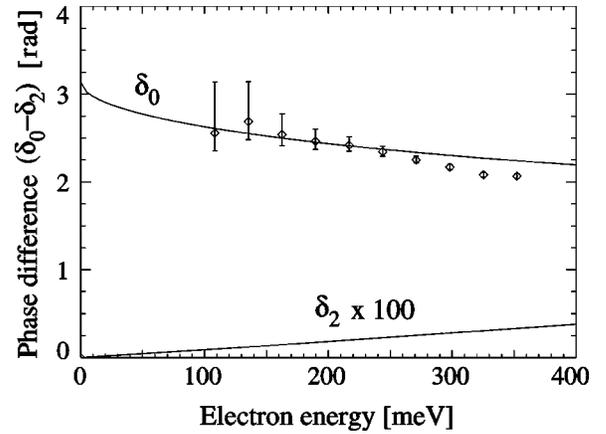

FIG. 8. Difference between the *s*- and *d*-wave elastic-scattering phases. The experimental data are shown by circles with error bars. The upper and lower solid lines represent predicted phases δ_0 and δ_2 calculated from Eqs. (12) and (13), respectively.

however, we can determine only the phase difference $\delta_0 - \delta_2$, a limitation which we discuss in the Appendix.

The dependence of $\delta_0 - \delta_2$ on the electron kinetic energy is shown in Fig. 8 together with the predictions from scattering theory. The phase δ_0 is analytically described in Ref. [32] by using the effective range approximation and it has the form

$$\cot\delta_0 = \frac{1}{p}\left(-\kappa + \frac{1}{2}\tilde{\rho}(\kappa^2 + p^2)\right), \quad (12)$$

where p is the electron momentum, $\tilde{\rho} = 2.646$ is a numerical parameter, and $\kappa = 0.2354$ is already introduced above. The phase δ_2 is calculated by using the expression

$$\tan\delta_L = \frac{\pi\alpha_d}{(2L+3)(2L+1)(2L-1)}p^2, \quad (13)$$

which is derived in Ref. [33] for elastic scattering on a model polarization potential and can be applied for the case of $L \geqslant 1$. Here $\alpha_d = 4.5$ a.u. is the dipole polarizability of the hydrogen atom. Figure 8 shows that in the given energy range the predicted phase δ_2 is much smaller than δ_0, and the experimental phase difference is well reproduced by δ_0 obtained from Eq. (12). We would like to notice that the phase difference extracted from an analogous fit of the simulated spectrum is in disagreement with the results of the scattering theory. This is not surprising because a Keldysh-like approach uses the Volkov function to describe the final state of the photoelectron. This function describes a free electron in the laser field, disregarding effects of the atomic core.

Figure 6 shows that at a certain kinetic energy the ADs experience a dramatic change characterized by a preferential electron emission perpendicular to the laser polarization. This behavior appears in both the experimental and theoretical spectra. It can be attributed to the quantum path interference, as we discuss it in detail in Sec. VI C. This specific modification of the angular distributions is also recently predicted by Borca *et al.* [8] and by Telnov and Chu [9].
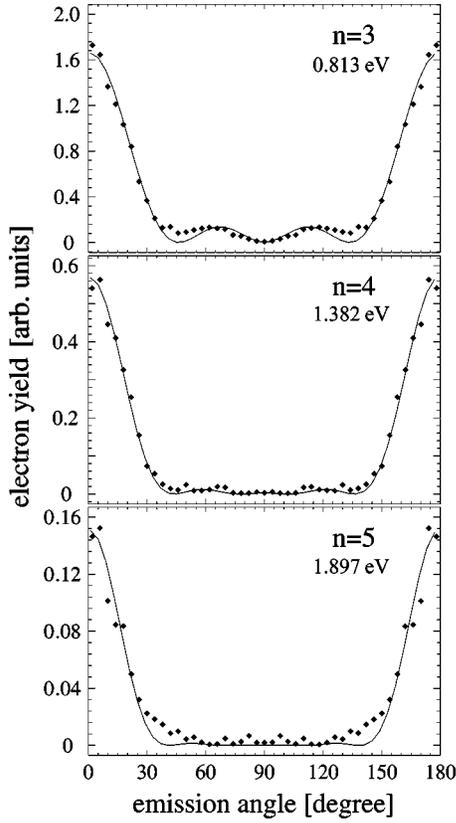
FIG. 9. ADs of channels $n=3$-5. Distributions are shown at kinetic energies where EPD channels acquire their maximal signal. The corresponding energy values are given in the figure. Dots represent experimental data, solid lines show simulated results obtained in previous chapter. Experimental and theoretical data are normalized to each other.

B. Angular distributions of higher-order channels

Figure 9 compares theoretical and experimental ADs of higher-order channels with the number of absorbed photons in the range from 3 to 5. The variation of an AD with energy in each of these channels is comparatively small. Therefore, the ADs are shown at energies where corresponding EPD peaks have their maximum signal, 0.813 eV ($n=3$), 1.382 eV ($n=4$), and 1.897 eV ($n=5$). With the increase in the number of absorbed photons the maximum value of the angular momentum in the final state is also increasing. This explains the decrease in width of maxima along the laser polarization, a tendency found in both experimental and the theoretical results. Experimental widths of these maxima are well reproduced by the theory. We should note that for odd photon channels small discrepancies appear at angles near 40° and 140°.

ADs of higher-order channels are fitted to a sum of Legendre polynomials using β coefficients as fit parameters [Eq. (A1)]. The set of β coefficients is not uniquely related to the set of partial-wave amplitudes of Eq. (10). This ambiguity is a consequence of the $2^{L_{max}/2}$ degeneracy in the solution of partial-wave amplitudes which we describe in the Appendix. Consequently, experimental results cannot be used to distinguish between different sets of complex partial amplitudes

TABLE I. β coefficients for channels $n=2$, 3, and 4.

Order	Energy	β coefficients				
n	(meV)	β_0	β_2	β_4	β_6	β_8
2	108	1.00	−1.22	0.13	0.11	0.01
2	325	1.00	−0.17	1.67	0.04	0.00
3	813	1.00	2.51	2.44	2.12	a
4	1382	1.00	3.39	3.67	2.62	0.73

[a]For final states of odd parity only p and f waves and their relative phase are included in the fit.

and further support from theory is required to identify the correct solution. In Table I we give the results of physically *correct* sets of β coefficients for the two-, three-, and four-photon channels, obtained by explicitly accounting for the theoretical constraint discussed in the Appendix.

C. Quantum interference

In this section we refer again to the dramatic change in ADs of the two-photon channel at low kinetic energies. When the electron momentum is small, the two saddle points in the plane of complex time acquire the simple form [6]: $t_1=(i\sinh^{-1}\gamma)/\omega$; $t_2=(\pi+i\sinh^{-1}\gamma)/\omega$, where γ is the Keldysh parameter introduced above. Real parts of $t_{1,2}$ define the two instants on the real time scale at which the electron is released into the continuum. It follows that electrons with low kinetic energies are emitted when the laser field has its maximum amplitude, at $t=0$ and $T/2$, where T is the period of the field oscillation. One can relate the times $t_{1,2}$ to the electron positions at the instant of photodetachment. Using the classical trajectory $r(t)=(F/\omega^2)\cos\omega t$ the electron positions are connected to the simple relation

$$r_{12}=\frac{2\kappa}{\omega}\frac{\sqrt{\gamma^2+1}}{\gamma}. \quad (14)$$

It was already discussed in Ref. [34] that results by Gribakin and Kuchiev in the limit of low kinetic energies [Eq. (11)] can be well described in terms of an intuitive two-slit interference picture. According to this picture, the ADs of photoelectrons are determined by the interference of two waves of wave vector $\mathbf{k}=\mathbf{p}/\hbar$ emitted with a time delay $T/2$ from two isotropic point sources, which are separated by the distance r_{12} and oriented along the laser polarization. A corresponding expression has the form

$$\frac{dw_n}{d\Omega}\propto|e^{i\mathbf{k}(\mathbf{r}-\mathbf{r}_1)}+(-1)^{n+\ell}e^{i\mathbf{k}(\mathbf{r}-\mathbf{r}_2)}|^2, \quad (15)$$

which implies that the interference pattern is observed at large distances compared to r_{12}. Figure 10 gives a schematic view to this situation.

The interference character depends on the parity of the final state determined by $n+\ell$. From Eq. (15) one can easily obtain the condition of destructive interference in the direction of laser polarization. For even parity of the final state,
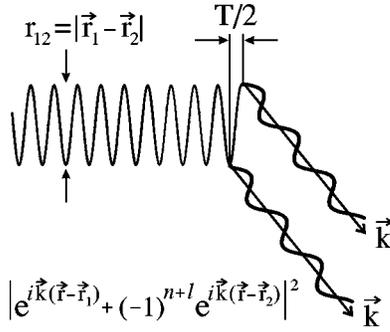
FIG. 10. Schematic picture of the origin of interference in electron emission from two laser induced point sources.

this situation occurs when the distance of source separation r_{12} is a half-integer number of the electron de Broglie wavelengths

$$\frac{2\kappa}{\omega}\frac{\sqrt{\gamma^2+1}}{\gamma} = \left(m+\frac{1}{2}\right)\lambda, \qquad (16)$$

where $\lambda = 2\pi/p$ and m is an integer number. Equation (16) describes the condition of destructive interference in the case of two-photon detachment of H^-, where the final state has even parity. This equation was solved to define the corresponding electron kinetic energy. One should take here into account that the electron energy is tuned by the ponderomotive shift. Thus, a given energy value E corresponds unambiguously to the field strength $F = 2\omega(E_2 - E)^{1/2}$, where $E_2 = 2\omega + E_0$ is the energy limit for the two-photon process. This field strength value should be used to evaluate the Keldysh parameter γ and, thus, the left-hand side of Eq. (16) should be considered as an energy dependent function. As a result of the solution of Eq. (16), we found that the destructive interference along the laser polarization occurs when electrons produced by two-photon detachment have a kinetic energy of 168.9 meV. This value is close to the experimental observation which shows that electrons of ≈ 130 meV energy are emitted preferentially perpendicular to the laser polarization.

A similar analysis is performed for the three-photon detachment channel. In this case a destructive interference along the laser polarization occurs when the separation distance r_{12} is an integer number of the electron de Broglie wavelengths. As a result, the destructive interference condition was found at two kinetic energies of 458.9 and 894.0 meV. These values, however, are of the order of the binding energy of the initial state and Eq. (14), which is valid in the limit of low energies $E \ll |E_0|$, cannot be applied here. A numerical analysis of the full expression [see Eq. (4)] shows that electron emission along the laser polarization is zero at $E = 344.5$ meV. This value falls into the region where the two-photon detachment has its maximum and, therefore, the interference effect in the three-photon channel is masked by the signal of the lower-order channel.

The simple picture of interference of two coherent electron emitters provides a useful and fully consistent two-slit analogy of the detachment process. It easily predicts the usual angular distributions observed, but offers a much simpler explanation than the interplay of quantum path trajectories in the formal approach [10]. It is also clear that for odd parity of the final state the detachment yield perpendicular to the polarization axis will interfere destructively. This is consistent with the property that odd partial-waves have a nodal plane perpendicular to the laser polarization axis. This is also in harmony with the Wigner threshold law in the limit of low kinetic energies.

VII. CONCLUSION

We present an experiment which employs a photoelectron imaging spectrometer in a fast negative-ion beam. Avoiding image distortion by diligent choice of experimental parameters we obtain the momentum-resolved angular distribution of electrons, photodetached from H^- in a strong infrared laser pulse. An accurate numerical procedure for the extraction of the energy-dependent differential photodetachment rate from the planar detector distribution is used in an analysis of partial-wave amplitudes and phases. Ambiguities associated in their extraction from experimental data are discussed.

The KFR theory of Gribakin and Kuchiev is used to simulate our experiment, explicitly accounting for the spatial and temporal laser intensity distribution, the saturation effect, and the ponderomotive shift. This enabled a determination of the differential photodetachment rate which can be directly compared with our experiment. The experimental verification of the KFR theory shows that it describes well the process of photodetachment in a strong laser field, reproducing all features of the rich experimental spectrum.

The Wigner law is a specific feature of a short-range potential, which signifies a fundamental difference between photodetachment and photoionization. We show here that the KFR theory does predict the Wigner threshold law.

Most intriguing, the KFR method predicts the profound quantum interference effect observed in the experiment. The interference case studied here can be interpreted in terms of a superposition of two complex electron trajectories. In the limit of low photoelectron momenta this effect has a surprisingly simple analogy of a double-slit interference. We suggest this stationary picture of quantum interference as an alternative interpretation of the photodetachment process of negative ions. This interpretation relies on the ratio of the de Broglie wavelength of the free electron and the separation distance between two isotropic coherent electron sources, which are located at the semiclassical amplitudes of the laser driven electron. We show that this interpretation is fully consistent with the Wigner threshold law and with the quantum path picture as motivated by the Feynman formalism.

APPENDIX: AMBIGUITY OF PARTIAL-WAVE AMPLITUDES AND CONSTRAINTS OF β COEFFICIENTS

The angular distribution of electrons formed in multiphoton detachment from an isotropic initial state by linearly polarized light has the form

$$\frac{d\Gamma_n}{d\Omega} = B \sum_{L \geq 0}^{2L_{\max}} \beta_L P_L(\cos\theta) \equiv B \sum_{L \geq 0}^{2L_{\max}} \alpha_L \cos^L\theta, \quad (A1)$$

where P_L are Legendre polynomials, and the normalization coefficient B is introduced so that $\beta_0 = 1$. The parity requirement implies the contribution of odd L to vanish. The right-hand side gives an equivalent functional form which represents a polynomial of order $2L_{\max}$ in the variable $x = \cos\theta$. The coefficients α_L and β_L obey a linear relationship. An equivalent representation of the polynomial in terms of products has the form

$$\frac{d\Gamma_n}{d\Omega} = B \, \alpha_{2L_{\max}} \prod_{i=1}^{2L_{\max}} (x - z_i), \quad (A2)$$

where z_i are complex roots of the polynomial and are related to the above coefficients in a nontrivial way. On the other hand, if the roots are known, the sets of α and β are easily computed by expanding Eq. (A2). Since the β coefficients are real, the roots of Eq. (A2) should emerge in complex conjugated pairs. In particular, if z_j is a root with $\mathrm{Im}(z_j) \neq 0$, then z_i^* represents another root. A special case is $\mathrm{Im}(z_j) = 0$. Then, $z_j^* = z_j$ and the root might emerge as twice degenerate. However, this is not an unambiguous consequence and such a root can also be nondegenerate. To check whether a degenerate root exists, we decompose the general form of Eq. (10) into a product of partial-wave amplitudes:

$$f_{p_n}(\theta)f_{p_n}(\theta)^* = \alpha_{2L_{\max}} \prod_{i=1}^{L_{\max}} (x - z_i) \prod_{i=1}^{L_{\max}} (x - z_i^*) \quad (A3)$$

and use the constraint that real roots of Eq. (A3) must appear as twice degenerate roots. This restricts the possible sets of the coefficients α_L, β_L. If the amplitude and roots are known, the more general expression

$$\tilde{f}_{p_n}(\theta) = \sqrt{\alpha_{2L_{\max}}} \prod_{i=1}^{L_{\max}} (x - \tilde{z}_i) \quad (A4)$$

with the zeroes $\tilde{z}_i$ chosen arbitrarily either as z_i or z_i^* produces exactly the same set of β coefficients. This latter property defines a $2^{L_{\max}}$ ambiguity for the partial-wave decomposition. If the parity of the final state is taken into account, the ambiguity reduces to $2^{L_{\max}/2}$ equivalent possibilities. Correct solutions are selected by forcing the coefficients of the opposite parity to vanish. For the case of even parity of the final state and $L_{\max} = 4$, the two complex equations

$$\tilde{z}_1 + \tilde{z}_2 + \tilde{z}_3 + \tilde{z}_4 = 0,$$

$$(\tilde{z}_3\tilde{z}_4 - \tilde{z}_1\tilde{z}_2)(\tilde{z}_1 + \tilde{z}_2) = 0 \quad (A5)$$

correspond to vanishing coefficients of the odd terms x and x^3. The nine independent quantities in Eq. (A4) [as well as α_L or β_L in Eq. (A1) with $L = 0,1,\ldots,8$] are reduced by the above equations to five independent fitting parameters. In the representation of partial-wave amplitudes in Eq. (10) these are given by the three moduli of partial-waves f_0, f_2, f_4 and the two phase differences $(\delta_0 - \delta_4),(\delta_2 - \delta_4)$. Thus, if one set of the latter is known, all $2^{L_{\max}/2}$ solutions can be obtained from Eq. (A4). A general solution of this ambiguity is impossible by an experiment using linearly polarized light. For the case $L_{\max} = 2$ only a phase ambiguity remains, preventing the experimental determination of $(\delta_0 - \delta_2)$ only modulo π with an undefined sign.

[1] L.F. DiMauro and P. Agostini, Adv. At., Mol., Opt. Phys. **35**, 79 (1995).
[2] C.J. Joachain, M. Dörr, and N. Kylstra, Adv. At., Mol., Opt. Phys. **42**, 225 (2000).
[3] L.V. Keldysh, Sov. Phys. JETP **20**, 1307 (1964).
[4] F.H.M. Faisal, J. Phys. B **6**, L89 (1973).
[5] H.R. Reiss, Phys. Rev. A **22**, 1786 (1980).
[6] G.F. Gribakin and M.Y. Kuchiev, Phys. Rev. A **55**, 3760 (1997).
[7] A. Lohr, M. Kleber, R. Kopold, and W. Becker, Phys. Rev. A **55**, R4003 (1997).
[8] B. Borca, M.V. Frolov, N.L. Manakov, and A.F. Starace, Phys. Rev. Lett. **87**, 133001 (2001).
[9] D.A. Telnov and Shih-I Chu, Phys. Rev. A **66**, 043417 (2002); **66**, 063409 (2002).
[10] P. Salières et al., Science **292**, 902 (2001).
[11] R. Kopold, W. Becker, and M. Kleber, Opt. Commun. **179**, 39 (2000).
[12] C. Blondel, M. Crance, C. Delsart, and A. Giraud, J. Phys. B **24**, 3575 (1991).
[13] M.D. Davidson, H.G. Muller, and H.B. van Linden van den Heuvell, Phys. Rev. Lett. **67**, 1712 (1991).
[14] H. Stapelfeldt, P. Balling, C. Brink, and H.K. Haugen, Phys. Rev. Lett. **67**, 1731 (1991).
[15] X.M. Zhao, M.S. Gulley, H.C. Bryant, C.E.M. Strauss, D.J. Funk, A. Stintz, D.C. Rislove, G.A. Kyrala, W.B. Ingalls, and W.A. Miller, Phys. Rev. Lett. **78**, 1656 (1997).
[16] M.S. Gulley, X.M. Zhao, H.C. Bryant, C.E.M. Strauss, D.J. Funk, A. Stintz, D.C. Rislove, G.A. Kyrala, W.B. Ingalls, and W.A. Miller, Phys. Rev. A **60**, 4753 (1999).
[17] H. Helm, N. Bjerre, M.J. Dyer, D.L. Huestis, and M. Saeed, Phys. Rev. Lett. **70**, 3221 (1993).
[18] A.T.J.B. Eppink and D.H. Parker, Rev. Sci. Instrum. **68**, 3477 (1997).
[19] T. Andersen, H.K. Haugen, and K. Hotop, J. Phys. Chem. Ref. Data **28**, 1511 (1999).

[20] P.A. Golovinski, I.Yu. Kiyan, Sov. Phys. Usp. **33**, 453 (1990).

[21] C. Bordas, F. Paulig, H. Helm, and D.L. Huestis, Rev. Sci. Instrum. **67**, 2257 (1996).

[22] R. Reichle, H. Helm, and I.Y. Kiyan, Phys. Rev. Lett. **87**, 243001 (2001).

[23] General methods of backprojection can handle the case of low values of the parameter ρ, when the entire image must be treated at once [24,25].

[24] M.J.J. Vrakking, Rev. Sci. Instrum. **72**, 4084 (2001).

[25] J. Winterhalter, D. Maier, J. Honerkamp, V. Schyja, and H. Helm, J. Chem. Phys. **110**, 11187 (1999).

[26] J. Weese, Comput. Phys. Commun. **69**, 99 (1992).

[27] For a better resolution figure, see our web page http://frhewww.physik.uni-freiburg.de/nip

[28] A.M. Perelomov, V.S. Popov, and M.V. Terent'ev, Sov. Phys. JETP **23**, 924 (1966).

[29] Z. Wang and D.S. Elliott, Phys. Rev. A **62**, 053404 (2000).

[30] E.P. Wigner, Phys. Rev. **73**, 1002 (1948).

[31] S.J. Smith and G. Leuchs, Adv. At., Mol., Opt. Phys. **24**, 157 (1988).

[32] T. Ohmura and H. Ohmura, Phys. Rev. **118**, 154 (1960).

[33] C. Laughlin and S.-I. Chu, Phys. Rev. A **48**, 4654 (1993).

[34] R. Reichle, I.Yu. Kiyan, and H. Helm, J. Mod. Opt. **50**, 461 (2003).